ELSEVIER

Investigating cerebral oedema using poroelasticity

John C. Vardakis [a], Dean Chou [b], Brett J. Tully [c], Chang C. Hung [d,e], Tsong H. Lee [d],
Po-Hsiang Tsui [f,g], Yiannis Ventikos [a,*]

[a] Department of Mechanical Engineering, University College London, Torrington Place, London WC1E 7JE, UK
[b] Institute of Biomedical Engineering & Department of Engineering Science, University of Oxford, Oxford OX1 3PJ, UK
[c] First Light Fusion Ltd., Begbroke Science Park, Begbroke, Oxfordshire OX5 1PF, UK
[d] Stroke Center and Department of Neurology, Chang Gung Memorial Hospital, Linkou Medical Center and College of Medicine, Taoyuan, Taiwan
[e] Department of Electrical Engineering, College of Engineering, Chang Gung University, Taoyuan, Taiwan
[f] Department of Medical Imaging and Radiological Sciences, College of Medicine, Chang Gung University, Taoyuan, Taiwan
[g] Medical Imaging Research Center, Institute for Radiological Research, Chang Gung University and Chang Gung Memorial Hospital, Taoyuan, Taiwan

ARTICLE INFO

ABSTRACT

Cerebral oedema can be classified as the tangible swelling produced by expansion of the interstitial fluid volume. Hydrocephalus can be succinctly described as the abnormal accumulation of cerebrospinal fluid (CSF) within the brain which ultimately leads to oedema within specific sites of parenchymal tissue. Using hydrocephalus as a test bed, one is able to account for the necessary mechanisms involved in the interaction between oedema formation and cerebral fluid production, transport and drainage. The current state of knowledge about integrative cerebral dynamics and transport phenomena indicates that poroelastic theory may provide a suitable framework to better understand various diseases. In this work, Multiple-Network Poroelastic Theory (MPET) is used to develop a novel spatio-temporal model of fluid regulation and tissue displacement within the various scales of the cerebral environment. The model is applied through two formats, a one-dimensional finite difference – Computational Fluid Dynamics (CFD) coupling framework, as well as a two-dimensional Finite Element Method (FEM) formulation. These are used to investigate the role of endoscopic fourth ventriculostomy in alleviating oedema formation due to fourth ventricle outlet obstruction (1D coupled model) in addition to observing the capability of the FEM template in capturing important characteristics allied to oedema formation, like for instance in the periventricular region (2D model).

1. Introduction

1.1. Hydrocephalus

Hydrocephalus (HCP) can be defined as the abnormal accumulation of CSF within the brain [1,7]. A balance between production and reabsorption exists, and it attempts to maintain the CSF pressure within a fairly narrow range of intracranial pressure (ICP) values [8]. HCP itself is not a singular pathological entity, but instead, a consequence of a variety of congenital and acquired disorders present within the central nervous system (CNS) [9]. HCP is classified with regards to whether the point of CSF obstruction or discreet lesion lies within the ventricular system (obstructive) and obstructs the flow before it enters the subarachnoid space (SAS) [10], or not (communicating). Normal Pressure Hydrocephalus (NPH) is a form of HCP that possesses no radiographically identifiable flow obstruction, however, there is evidence of craniomegaly and ventriculomegaly taking place [11,12].

1.2. Cerebral oedema

Cerebral oedema refers to swelling produced by expansion of the interstitial fluid volume (or an increase in water content above the normal level of brain water content) and is a common response to primary brain insult [13,14]. Cerebral oedema is usually classified into the major subtypes: cytotoxic, vasogenic, interstitial or combined [13–16]. Most brain injuries however involve a combination of these subtypes, making overall classification difficult. Interstitial oedema is considered a consequence of impaired CSF outflow (as in obstructive HCP), leading to increased intraventricular pressure and a compromised ependymal lining. Subsequently, an increase in transependymal CSF flow migration into the parenchyma and the periventricular regions take place. Osmotherapy is a well-known (albeit
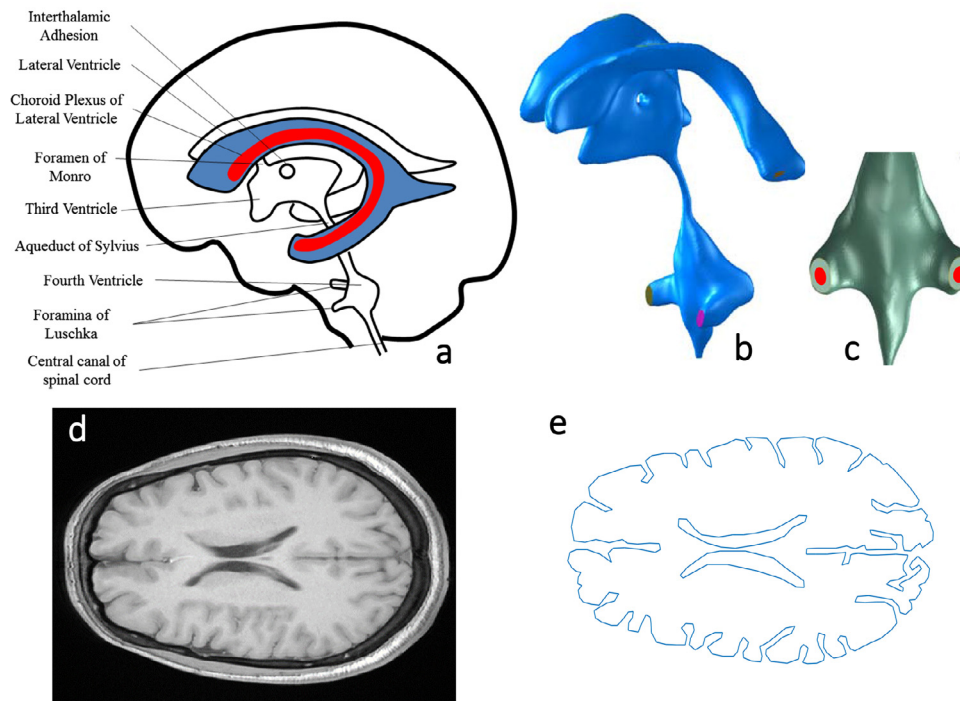
Fig. 1. CSF containing cavities, image-based reconstruction of the ventricular morphology and MRI slice used to create the 2D region of interest. (a) CSF circulates through the four brain ventricles and in the subarachnoid space surrounding the brain and spinal cord. A sizeable proportion is produced in the choroid plexus of the lateral, third and fourth ventricle regions. A schematic depiction of the *C* shaped choroid plexus is shown for the left lateral ventricle. (b) The final ventricular geometry used for the 1D-3D coupled simulations. (c) Location and approximate size of outlet (red oval) created to mimic EFV at the bilateral Foramina of Luschka, situated on the fourth ventricle. (d) MRI slice used to create the parenchymal region in addition to extracting the ventricles. (e) Outline of the parenchymal region that was discretized for the 2D FEM simulations.

controversial) non-invasive treatment of oedema [16]. Aquaporins (AQPs) are widely considered as key players in the resolution of oedema, owing to their regionally distinct distribution [15,17,18]. More specifically, AQP4 is believed to evoke an interrelation between cerebral oedema and neuroinflammation [17,19]. The recently coined glymphatic system and its regulation is also considered to have a potentially active role in developing key therapies for oedema. Thrane et al. [20] for instance, suggest that vasogenic oedema is representative of prolonged increase of glymphatic fluid influx that assists in paravascular leukocyte and cytokine delivery. In this work, interstitial oedema is investigated, as this type of oedema is borne out of ventriculomegaly, and targets the periventricular region. In addition, a simple relationship that allows for small variations of permeability in the MPET model which account for the swelling characteristics induced by AQP4 (see Eq. (5)) is also included within the MPET framework.

1.3. Endoscopic ventriculostomy for alleviating oedema and hydrocephalic symptoms

Many recommend that endoscopic third ventriculostomy (ETV) be suggested as a first-line treatment to all patients that require management of HCP [21–27]. ETV involves passing an endoscope into either lateral ventricle (see Fig. 1a) via a burr hole in the frontal region. The enlarged third ventricle will have its thin floor stretched due to HCP, and it will resemble a translucent membrane. The floor is perforated and enlarged via various means such as a balloon catheter, Grotenhuis perforation [28] or Decq forceps [29], thus creating an artificial opening into the basal subarachnoid spaces. Ultimately, this is a natural way of draining excess CSF. Similarly to ETV, endoscopic fourth ventriculostomy (EFV) involves puncturing and dilating the occluded membranes due to atresia of the foramina of the fourth ventricle. EFV may prove to be a sound alternative treatment (as ETV is considered the preferred option for various types of Fourth Ven-

tricular Outlet Obstruction (FVOO) [30] and sequestrated or trapped fourth ventricle [23]) in cases where ETV cannot be considered.

1.4. Pertinent models of oedema using small-strain poroelasticity

Nagashima et al. [31–34] modeled vasogenic brain oedema, using the finite element method. The authors in the aforementioned work [31] used a set of parameter values and boundary conditions that do not coincide with the most recent literature, notably the use of a Poisson's ratio (of 0.47), and Young's modulus (in the work presented here, a value of around 584 Pa [35] is used). Peña et al. investigated the biomechanics of acute obstructive HCP and periventricular lucency (PVL) through the use of a two-dimensional biphasic poroelastic model solved using the FEM [36]. Further references to work on existing models of the CSF compartment are given in a previous publication by the same authors [3]. A thorough and recent review on the mechanics of the brain is also given by Goriely et al. [16].

2. Methods

2.1. Geometry

Imaging was performed on a 1.5T GE Signa system (Waukesha, WI, USA) and a T2 weighted imaging sequence was used for obtaining the brain anatomy data of a male volunteer in his 60s. The acquired voxels were manually segmented for the ventricular system using Amira (Mercury Computer Systems, San Diego, CA, USA) and the raw segmented geometry from this process was converted to a Stereo Lithography (STL) file. In order to preserve key anatomical features, smoothing of the STL file was executed using Blender (The Blender Foundation, www.blender.org), as it provides the option of locally smoothing parts of a mesh, in addition to its global smoothing capabilities. Alternating between local and global smoothing was required in order to keep the angle between faces within expected limits. The

final geometry is seen in Fig. 1b. Spatially accurate representations of the choroid plexuses were also used, within the lateral, third and fourth ventricles (see [3]). These anatomically accurate geometries were used to conduct the coupled 1D MPET-CFD based simulations.

For the 2D FEM based MPET template, a realistic polygonal representation of a cross section of the cerebral ventricles and parenchymal region was used (see Fig. 1d and e) as the region of interest and obtained from the same MRI sequence described above. A total of 323 coordinate pairs were used to represent the parenchymal region and subtracted ventricles.

The poroelastic framework that will be used to interrogate the basic processes that underlie the pathophysiology of FVOO along with interstitial oedema will now be described.

2.2. Multicompartmental poroelastic formulation

2.2.1. Multiple-network poroelastic theory

Poroelasticity is known to have numerous applications in biomedical engineering as well as soil mechanics and reservoir engineering. The classical form of Biot's consolidation model is described for an isotropic and incompressible solid matrix and homogenous porous medium [37,38]. For a simple poroelastic medium to be defined, an equilibrium equation is needed to define elastic deformation, Darcy's law is used to model fluid flow, and finally mass conservation is also required. Assuming the porous medium lies within the bounded domain $\Omega \subset \mathbb{R}^n$, one may cast equations to be solved for the mean displacement of particles forming the solid matrix, $\mathbf{u}$, and the scalar pore pressures of the extended multicompartmental porous medium (p^a, p^c, p^e, p^v), which is defined through multiple-network poroelastic theory (MPET). Biologically, the quadruple MPET system is derived by accommodating a high pressure arterial network (a), lower pressure arteriole/capillary network (c), CSF/ISF network (e) and finally a venous network (v) which satisfies the system in Eqs. (1) and (2). The intracranial pressure is represented by the CSF/ISF compartment in the MPET model.

$$\nabla \cdot \sigma_{ij} = 0$$

$$\sigma_{ij} = (\lambda \epsilon_{kk} - \sum_{A=a,e,c,v} \alpha^A p^A)\delta_{ij} + 2\mu\epsilon_{ij}$$

$$\epsilon_{ij} = \frac{1}{2}(\partial u_i/\partial x_j + \partial u_j/\partial x_i) \qquad (1a\text{–}c)$$

$$\left.\begin{array}{l} \frac{\partial}{\partial t}(c_\varepsilon^a p^a + \alpha^a \epsilon_{ii}) + \nabla \cdot [f^a] = \dot{S}_a \\ \frac{\partial}{\partial t}(c_\varepsilon^c p^c + \alpha^c \epsilon_{ii}) + \nabla \cdot [f^c] = \dot{S}_c \\ \frac{\partial}{\partial t}(c_\varepsilon^e p^e + \alpha^e \epsilon_{ii}) + \nabla \cdot [f^e] = \dot{S}_e \\ \frac{\partial}{\partial t}(c_\varepsilon^v p^v + \alpha^v \epsilon_{ii}) + \nabla \cdot [f^v] = \dot{S}_v \end{array}\right\} x \in \Omega, \; 0 < t \le T$$

$$where: f^A = -\frac{k^A}{\eta^A}(\nabla p^A) \qquad (2a\text{–}e)$$

In the above equations, the symmetric tensor σ_{ij}, is the standard elastic stress tensor (effective stress), p^A is the scalar pore pressure in each fluid compartment, ϵ_{ij} is the linearized strain tensor, $\epsilon_{ii} = \nabla \cdot \mathbf{u}$ is the dilatation, λ and μ are the Lamé coefficients of the elastic medium, α^A is the Biot–Willis coefficient for each fluid compartment, superscript A represents the relevant fluid compartment a, e, c or v, f^A is the Darcy flux for each compartment A that is used to describe the transport of the four percolating fluid networks within the solid matrix. Since this is an isotropic porous medium, the intrinsic permeability tensor is the same for all diagonal elements ($k_{ij} = 0, i \ne j$) in each of the four compartments. η^A is defined as the viscosity of each fluid compartment. Through mass conservation, Eq. (2)a–d are the pore pressure equations for each of the four compartments and

are defined by c_ε, the inverse of the specific storage (a measure of the released fluid volume per unit pressure in the control volume at constant strain for each fluid compartment), and $\dot{S}_A$, the external pressure and time-dependent (owing to the temporal evolution of the boundary conditions) source ($\dot{S}_A > 0$) or sink ($\dot{S}_A < 0$) for each compartment (rate of fluid transfer between networks $b \to a$).

In Eq. (2)a–d above: $\dot{S}_a = -|\dot{s}_{a\to c}|$, $\dot{S}_c = |\dot{s}_{c\to e}| - |\dot{s}_{e\to v}|$, $\dot{S}_e = |\dot{s}_{a\to c}| - |\dot{s}_{c\to e}| + |\dot{s}_{c\to v}|$, $\dot{S}_v = |\dot{s}_{e\to v}| + |\dot{s}_{c\to v}|$, where $\dot{s}_{b\to a}$ are the network transfer coefficients. The transfer of fluid between the four fluid networks is required to obey the law of continuity for the entire system, and so directionality between fluids compartments must be accurately specified (Fig. 2a). It should be noted that at the current state of development of the model, the source/sink terms are of the form $\dot{S} = \omega_{ij}(p^j - p^i)$ which implies that a hydrostatic pressure gradient drives the transfer, and where ω_{ij} represents the transfer coefficient scaling the flow from network j to network i. The magnitudes of these transfer coefficients are given in Table 1.

2.2.2. Boundary conditions

The MPET system is completed with the following boundary conditions for each of the four fluid compartments, where $\partial\Gamma_s$ and $\partial\Gamma_v$ are boundaries at the skull and cerebral ventricles respectively, and $\mathbf{n}$ is the outward unit normal vector:

On the skull:

$$\mathbf{u} = \mathbf{0} \quad on \quad \partial\Gamma_S,$$

$$p^a|_{\partial\Gamma_S} = p_{bpA} \quad on \quad \partial\Gamma_S,$$

$$\nabla p^c \mathbf{n}|_{\partial\Gamma_S} = 0 \quad on \quad \partial\Gamma_S,$$

$$p^v|_{\partial\Gamma_S} = p_{bp} \quad on \quad \partial\Gamma_S,$$

$$p^e|_{\partial\Gamma_S} = p^v|_{\partial\Gamma_S} + \eta^e RQ_o \quad on \quad \partial\Gamma_S,$$

$$\frac{p^e|_{\partial\Gamma_S} - p_{bp}}{\eta^e R} = \frac{\pi d^4}{128\eta^e L}(p^e|_{\partial\Gamma_V} - p^e|_{\partial\Gamma_S})$$

$$+ \oint_S \left(-\frac{k^e}{\eta^e} \cdot \nabla p^e\right).\mathbf{n}ds \quad on \quad \partial\Gamma_S. \qquad (3a\text{–}f)$$

On the ventricle surface:

$$-p^e|_{\partial\Gamma_V}\mathbf{n} = \sigma_{ij} \cdot \mathbf{n} \quad on \quad \partial\Gamma_V,$$

$$\nabla p^a \mathbf{n}|_{\partial\Gamma_V} = 0 \quad on \quad \partial\Gamma_V,$$

$$\nabla p^c \mathbf{n}|_{\partial\Gamma_V} = \frac{Q_p}{\kappa_{c-vent}} \quad on \quad \partial\Gamma_V,$$

$$\nabla p^v \mathbf{n}|_{\partial\Gamma_V} = 0 \quad on \quad \partial\Gamma_V,$$

$$\dot{V} = Q_p - \frac{\pi d^4}{128\eta^e L}(p^e|_{\partial\Gamma_V} - p^e|_{\partial\Gamma_S})$$

$$- \oint_V \left(-\frac{k^e}{\eta^e} \cdot \nabla p^e\right).\mathbf{n}ds \quad on \quad \partial\Gamma_V. \qquad (4a\text{–}e)$$

Since this is an adult brain that is being taken under consideration; a rigid wall approximation can be envisaged stemming from the elimination of layers like the dura mater and scalp, giving rise to Eq. (3)a. For continuity of stresses, the poroelastic stress present in the brain's tissue must balance the ventricular pressure exerted by the CSF within the inner ventricular wall (Eq. (4)a). Based on vascular wall-thickness arguments, there is no flow into or out of the arterial and venous blood networks (Eq. (4)b and d), whilst CSF being produced from the blood results in a pressure drop in the arteriole/capillary blood network, where $\kappa_{c\to vent}$ represents the capillary network resistance to the flow from the capillary compartment (Eq. (4)c). The blood pressures are given by arterial and venous blood pressures in Dirichlet form on the skull (Eq. (3)b and d), where p_{bpA} and p_{bp} are the arterial blood pressure and blood pressure in the sagittal sinus respectively. At the skull, CSF absorption causes a pressure rise dependent on the resistance to absorption via the arachnoid granulations, R, and the rate of CSF efflux at the skull is given by
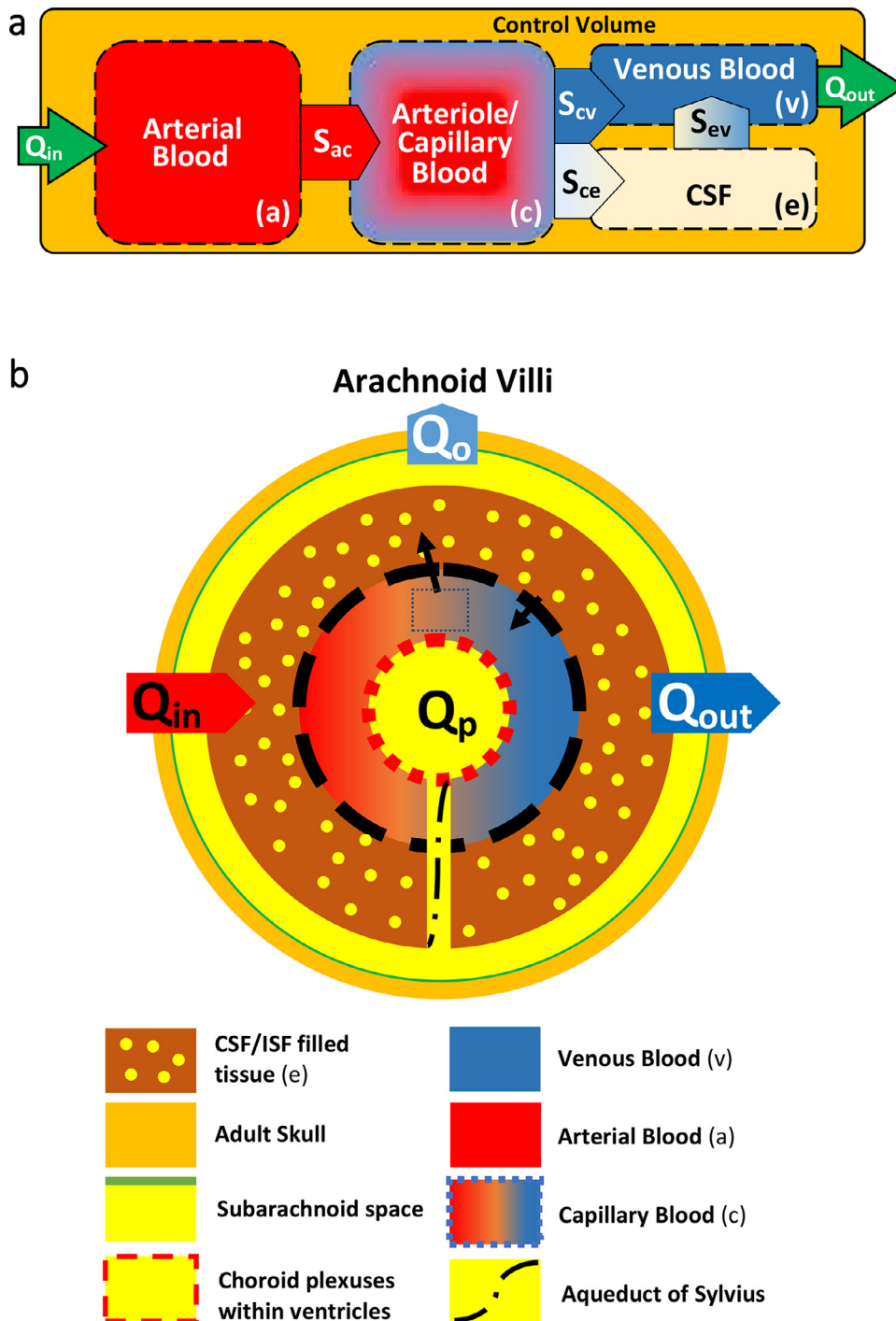
Fig. 2. The fluid transfer restrictions placed between the four compartments and spherical shell representation of parenchymal tissue. (a) Flow is prohibited between the CSF/ISF and arterial network, whilst directional transfer exists between the $a \rightarrow c$, $c \rightarrow v$, $c \rightarrow e$ and $e \rightarrow v$ networks respectively. (b) Parenchymal tissue is represented using a spherical shell representation. The ventricles are connected to the subarachnoid space via an anatomically accurate cerebroventricular system (Fig. 1b). The two arrows in the figure denote directional transfer between $c \rightarrow e$ and finally $e \rightarrow v$. The legend below the schematic depicts some of the finer features of this representation.

Q_o. CSF is assumed to be produced at a constant rate, Q_p within the ventricles.

The absorption of CSF is assumed to take place in the bloodstream near the skull, where the rate of absorption is described by the left hand side of Eq. (3)f. The amount of fluid absorbed into the blood stream must be equal to the amount of fluid flowing to the skull via the aqueduct in addition to the amount of fluid passing through the brain parenchyma. This balance of flow rates completes the right hand side of Eq. (3)f.

Directional restriction of the transfer of water between fluid networks is shown in Fig. 2a. Table 1 gives the complete list of all parameters used to execute the MPET model.

The following relationship was used (to alleviate the constraint of a unique permeability for the CSF/ISF compartment) to qualitatively account for AQP4 swelling characteristics for the 1D model:

$$k^e = \left(\frac{k^{e0}}{\eta^e} \right) \left(1 - \frac{\Delta P_k}{P_{ref}} \right) \tag{5}$$

Table 1

List of the parameter values used in the MPET framework. The majority of parameters in this table have been used in previous studies [1–6].

Parameter	Value	[Units]	Parameter	Value	[Units]
r_v	3	cm	ω_{ac}	1.5×10^{-19}	$m^2 N^{-1} s^{-1}$
r_M	10	cm	ω_{cv}	1.5×10^{-19}	$m^2 N^{-1} s^{-1}$
L	7	cm	ω_{ev}	1.0×10^{-13}	$m^2 N^{-1} s^{-1}$
d	3	mm	ω_{ce}	2.0×10^{-19}	$m^2 N^{-1} s^{-1}$
E	584	Nm^{-2}	$k^{a,c,v}$	1.0×10^{-10}	m^2
p_{bp}	650	Nm^{-2}	$k^e (= k^{e0})$	1.4×10^{-14}	m^2
p_{bpA}	13.3×10^3	Nm^{-2}	K	649	Nm^{-2}
R	8.5×10^{13}	m^{-3}	λ	505	Nm^{-2}
Q_p, Q_o	5.8×10^{-9}	$m^3 s^{-1}$	G	216	Nm^{-2}
$\kappa_{c \rightarrow vent}$	6.4×10^{-4}	$m^5 s k g^{-1}$	c_ε	4.5×10^{-10}	$m^2 N^{-1}$
η^e	8.9×10^{-4}	Nsm^{-2}	ν	0.35	
$\eta^{a,c,v}$	2.67×10^{-3}	Nsm^{-2}	β	0.99	
ρ^e	997	$kgsm^{-3}$	$\alpha^{a,e,c,v}$	0.99	

In the above equation, k^{e0} is the base permeability (see Table 1). This permeability was made to vary within the interval: $10^{-14} \leq k^{e0} \leq 10^{-13}$. ΔP_k is the pressure difference between the compartmental CSF/ISF pressure and a reference pressure, P_{ref}, whose value was chosen to be 1 kPa. This is similar to the method adopted in previous work from the same authors [3]. A constant permeability (equal to k^e) was used for the 2D simulations.

Finally, initial conditions are also imposed for the transient system when considering the finite element based template. The initial conditions are the solution of the quasi-steady system ($\mathbf{u}(\mathbf{x}, 0)$, $p^a(\mathbf{x}, 0)$, $p^c(\mathbf{x}, 0)$, $p^e(\mathbf{x}, 0)$, $p^v(\mathbf{x}, 0)$) when $\partial/\partial t \rightarrow 0$ in Eq. (2)a–d, and are used along with an implicit backward Euler step to feed the two starting vectors of the 2nd order accurate BDF method described in the last sub-section of Section 2.

Finally, the increment of fluid content for each compartment, ζ^A, in terms of strain, ϵ reads as:

$$\zeta^A = \alpha^A \left[\epsilon + \frac{(1 - \alpha^A \beta)}{K\beta} p^A \right] \tag{6}$$

In Eq. (6) above, the parameter β is defined as Skempton's coefficient. It denotes the measure of the distribution of the applied stress between the solid matrix and fluid. A value of $\beta \approx 1$ represents a saturated mixture where the applied load is nearly entirely supported by the CSF/ISF.

2.3. Numerical methods

2.3.1. Finite difference – finite volume 1D MPET coupling

The final system of Eqs. (1)a–c and (2)a–d utilizes a one-dimensional, spherically symmetric geometrical representation. The parenchyma of an adult brain is represented as a spherical shell (see Fig. 2b). The outer radius of this shell is given by r_M, whilst the lumped representation of the lateral ventricles is represented by another spherical shell with radius r_v. The third and fourth ventricles along with the Sylvian aqueduct are assumed to be connected to the SAS. The geometry representing all the features of the ventricles arise from a volunteer scan, and is outlined in Section 2.1. Additional assumptions include the notion that HCP has a long time scale for development, of the order of days, weeks or even years (if one considers the progressive acute and chronic case). It is therefore evident that an assumption of a quasi-steady system is not unrealistic. This quasi-steady constraint imposes $\partial/\partial t \rightarrow 0$. When executing the CFD simulations to determine the CSF flow dynamics through the ventricular system, the flux of CSF exiting the outlets is used to replace the Hagen–Poiseuille assumption in Eqs. (3)f and (4)e.

2.3.2. Finite difference – finite volume MPET coupling implementation

The governing MPET equations are solved with an implicit second-order central finite differences scheme on the midpoints and for-ward/backward Euler used on the boundary nodes. The quasi-steady time discretization (for the temporally dependent terms in the boundary conditions) is performed via a first-order Euler approach. Flow through the multidimensional aqueducts and choroid plexuses is solved using the multiphysics software CFD-ACE+ (ESI Group, Paris, France), along with central spatial differencing, an algebraic multigrid scheme and the SIMPLEC pressure–velocity coupling [39]. The coupling between the poroelastic solver and the flow solver is achieved through CFD-ACE+ user-defined FORTRAN subroutines. Mesh generation for the 3D cerebroventricular volume and choroid plexuses was achieved via the use of CFD-VisCART (ESI Group, Paris, France), which is an unstructured adaptive Cartesian grid generation system. For the entire system (ventricles and choroid plexuses) over 2 million cells were used for each simulated case. Grid independence analysis has shown that this resolution is adequate for the problem at hand. The MPET template used a grid discretization of 81 nodes, consistent with previous studies by the same authors [1–3,40].

2.3.3. The MPET 2D finite element formulation

In two dimensions, the MPET equations and the associated boundary conditions are solved using a FEM scheme. The need to adopt a FEM template arises from the use of the complex geometry of the parenchymal space and ventricles (Fig. 1e). The use of the aforementioned geometry naturally requires the use of local mesh refinement. The FEM in known to outperform the FDM method when considering these two important factors.

Let $\Omega \subset \mathbb{R}^2$ be a domain with Lipschitz continuous boundary $\partial\Omega$ and unit outward normal $\mathbf{n}$. The triangulation $\mathcal{T}$ of Ω is a set $\{T\}$ of triangles T, where $\Omega = \cup_{T \in \mathcal{T}} T$. The intersection of two triangles is either an edge, empty or a corner. The mesh does not contain any hanging nodes. The family of triangular partitions is assumed to be shape-regular and quasi-uniform in order to optimally approximate the finite element domains in this study. We subsequently arm the polynomial functional space $\wp$ on $\mathcal{T}$ with shape functions for linear and quadratic Lagrange triangles, which possess canonical bases of $\{1, r, s\}$ and $\{1, r, s, r^2, rs, s^2\}$, respectively. We isoparametrically map the triangular elements in the manner $(x, y) \longmapsto (r, s)$.

For the 2D geometry, MATLAB was used to construct the Delaunay triangulation. The total number of triangles for the anatomical geometry was 56,416. For the latter geometry, the number of nodes for the linear displacement elements was 29,363, whilst for the quadratic elements used for the fluid phases this increased to 115,143. The minimum and maximum simplex quality was 0.61 and 0.99, respectively. For the FEM formulation, one relaxes the spherical assumption that was used in the FDM based template (Fig. 2b). Spatial discretization of the system through the weak form of the liquid and solid phases is conducted via the standard multiplication of relevant test functions and integrating by parts, and finally applying the boundary conditions. The time integration is obtained via a spatial-semi discretization of the liquid phases, where the space discrete solution is obtained for the four compartments via the solution of a system of ordinary differential equations which satisfy time-dependent nodal values. In this context, the implicit backward-Euler method is used with a time step τ for the fluid phases,

$$c_\varepsilon^A p^A(\mathbf{x}, t) + \alpha^A \nabla \cdot \mathbf{u}(\mathbf{x}, t) + \tau \nabla \cdot [f^A(\mathbf{x}, t)]$$
$$= \tau \dot{S}_A + \alpha^A \nabla \cdot \mathbf{u}(\mathbf{x}, t - \tau) + c_\varepsilon^A p^A(\mathbf{x}, t - \tau) \tag{7}$$

in order to accommodate one of the two (the second being the homogeneous steady state solution of the MPET system) starting vectors required for the second order accurate Backward Difference Formula, BDF(2), which is well suited to stiff problems in addition to being able to accommodate large step-sizes. Gauss quadrature weights of precision four were also used in the template. The Transpose-Free Quasi Minimal Residual Method (TFQMR) iterative method was used to solve the sparse system [41]. Since the TFQMR method is part of the QMR family of iterative methods, sparse incomplete LU factorization
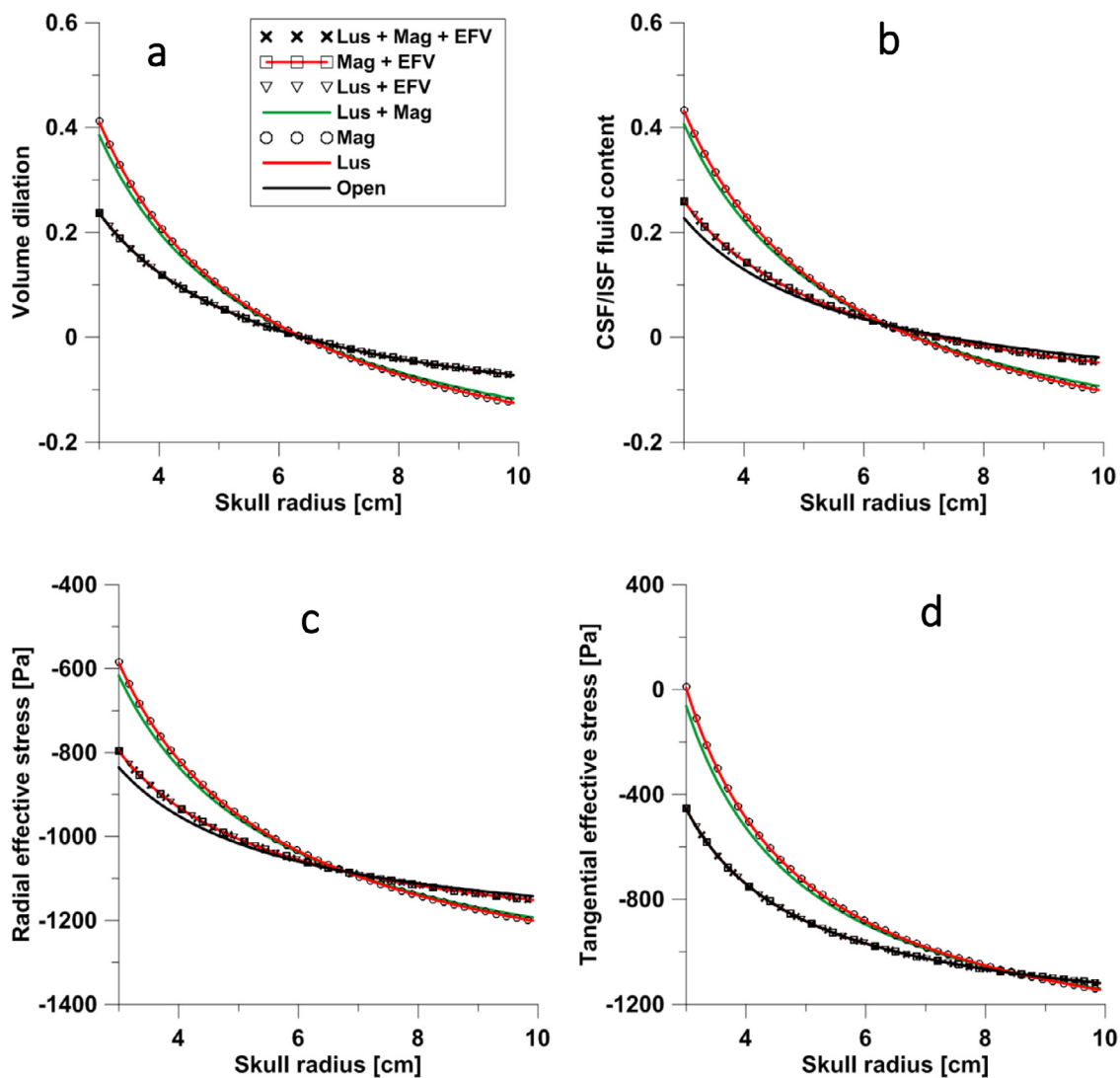
Fig. 3. Volume dilation, CSF/ISF fluid content and components of effective stress for different cases of four ventricle outlet obstruction and applied fourth ventriculostomy. (a) Variation of volume dilation within the parenchymal tissue from the ventricles (3cm radius) to the skull (10cm radius). (b) Depicts the variation of CSF/ISF fluid content (oedema) within the parenchymal tissue. (c) Radial component of effective stress. (d) Tangential component of effective stress.

was deemed a suitable preconditioner in order to help accelerate the rate of convergence, in addition to improving the spectral properties of the system matrix.

3. Results

The following sections outline the results garnered from the 1D coupled FDM-CFD simulation and 2D FEM templates.

In Fig. 3a it can be seen that atresia at the foramina of Luschka or foramen of Magendie can increase the volume dilation by approximately 71%, from 0.24 to 0.41. Blockage of all the outlets increased the dilation by just under 58%, to 0.38. Applying EFV reduced the dilation for all forms of atresia to approximately the same level of 0.24. What is also visible from the plots is that once a skull radius of 6.5 cm is exceeded, the dilation of parenchymal tissue is compressive until the periphery of the skull. The difference in compression between the patent aqueduct and cases of atresia is most attenuated at the region of the skull, whilst the application of EFV alleviates the effect, and reduces the compression to around −0.07.

Fig. 3b shows a similar trend for the level of oedema (or fluid content, ζ^e, see Eq. (6)). Atresia of the aforementioned foramina increases the level of interstitial oedema (on and near a skull radius of 3 cm) by 87% (Luschka), 87% (Magendie) and 78% (tri-exit closure).

Applying EFV once again reduces the level of interstitial oedema to levels close to the patent case, with a difference of around 13% in comparison to the patent aqueduct. It can be seen that fluid is squeezed out ($\zeta^e < 0$) of the parenchyma after a skull radius of around 6.5 cm. Application of EFV reduced the amount of CSF/ISF being squeezed out by up to 53%.

Fig. 3c and d depicts the radial and tangential effective stresses. A trend of larger transparenchymal difference reduction can be seen when application of atresia is considered. For the patent aqueduct, the radial and tangential transparenchymal difference in effective stress is just over 307 and 664 Pa, respectively. Atresia of the foramen of Magendie induced the largest difference in radial and tangential effective stress, with just over 614 and 1156 Pa, respectively. Near recovery to nominal (patent aqueduct) levels is witnessed with the application of EFV in radial effective stresses and full recovery for tangential effective stresses.

Fig. 4a and b shows the u and v components of displacement after 5 s of simulation. The displacement for both components varies (maximum and minimum) from 0.27 to -0.28 mm, and 0.32 mm and -0.22 mm respectively.

Fig. 4c depicts the CSF/ISF fluid increment solution after 5 s of simulation. Fluid swelling can be seen in the periventricular region in addition to areas of high concavity. More pronounced qualitative
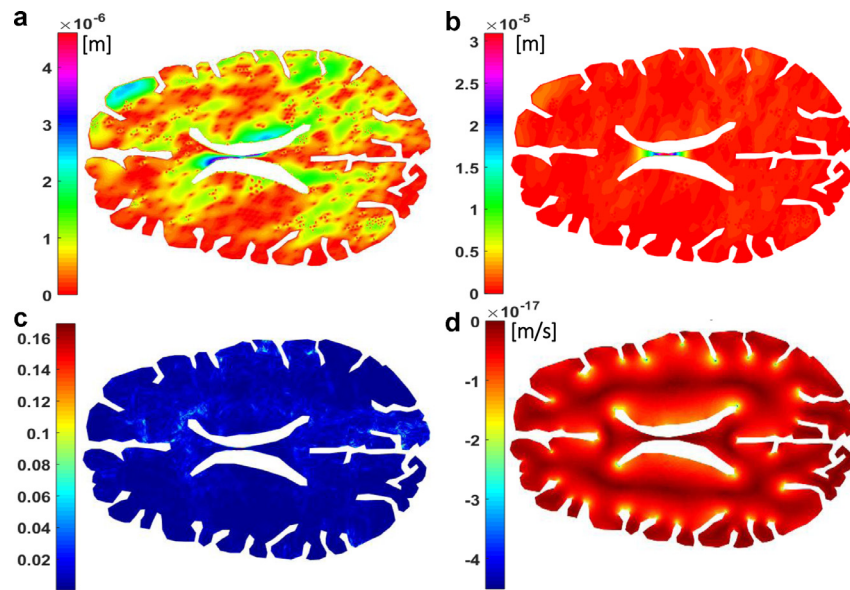
Fig. 4. Components of ventricular displacement, capillary filtration velocity and CSF/ISF fluid increment. (a) The **u** component of displacement within the 2D geometry, when $\alpha_e \approx 1$. (b) The **v** component of displacement within the 2D geometry, when $\alpha_e \approx 1$. (c) CSF/ISF fluid increment. This solution field for both displacement components changes fairly rapidly with total simulated time (in addition to time increment), which possesses smoother transitions between ventricles and parenchymal periphery. c_ε also plays an important role in this evolution. (d) Darcy velocity of the capillary compartment. Velocities of the order of -4.5×10^{-17} m/s can be found in the lower right ventricle (posterior horn), whilst the darker regions are of the order of 10^{-18}–10^{-19} m/s.

trends are witnessed for the Darcy velocity of the capillary compartment (Fig. 4d), and it is noted that flow takes place opposite to the direction of increasing pressure gradient. The parenchymal region offers velocities of lower orders of magnitude. Velocities of the order of -4.5×10^{-17} m/s can be found in the posterior horn, whilst the darker regions are of the order of 10^{-18}–10^{-19} m/s. In the CSF/ISF compartment (not shown), higher velocities (-6 μm/s) can be found in the same regions (due to the pressure boundary conditions).

Fig. 5a–d shows the pressure fields for the four fluid compartments. For the ISF/CSF compartment (Fig. 5a), a peak pressure of 1645.9 Pa can be found on the ventricles, whilst, the minimum is on the periphery of the parenchyma, at 1088.77 Pa. For the venous compartment (Fig. 5b), a peak pressure of 650 Pa is found in the parenchymal periphery, whilst pressure values of 80–200 Pa can be found closer to the ventricles. The arterial compartment (Fig. 5c) displays a similar trend, however the high peak pressure of 13,300 Pa reflects the boundary conditions for this compartment. Fig. 5d shows the capillary compartment pore pressure. Peak values (0.16 μPa) exist within the core of the parenchyma, with lower magnitudes (approaching zero) found around the periphery.

4. Discussion

It is evident from Fig. 3a–d, that FVOO induces the formation of interstitial oedema (in the region on and near a skull radius of 3 cm) when observing that changes in volume dilation and CSF/ISF content. At a skull radius of 3 cm, the positive values of volume dilation and fluid content indicate tissue damage and as a consequence fluid accumulation, whilst tissue closer to the skull (skull radius of 6.5–10 cm), the negative values indicate a compressed solid matrix and therefore fluid being squeezed out of the parenchyma. These results qualitatively correlate with other work in the literature [3,42].

It is clear from the simulations that these effects can be alleviated when considering the EFV surgical technique, reducing the periventricular levels of volume dilation and CSF/ISF content to levels just above the recorded results for the unobstructed aqueduct with respect to the ventricles, and with a finite attenuation of drainage with respect to the skull.

Although both sets of radial and tangential effective stresses (Fig. 3c and d) are compressional (also due to the pressure evolution of the CSF/ISF compartment) in nature (and as observed by Levine [43–45]), the impact of FVOO leads to periventricular tension until a skull radius of 6.5 cm. From this point until the skull, the nature of the radial effective stresses is purely compressional. The same is true for the tangential effective stress, however the solely compressional nature commences closer to the skull, at a skull radius of around 8.5 cm. The transparenchymal difference in effective stress is minimized with the aid of EFV. An interesting result was that the radial component of the effective stress does not fully return to the level of the open aqueduct, whilst the tangential component nearly fully recovers. This is also displayed in the results shown by the volume dilation. The fact that a complete tri-exit closure did not correspond to even higher levels of volume dilation and effective stress than individual outlet atresia highlights the need to further investigate the role of the central canal in such circumstances, in addition to the likelihood that convective CSF/ISF fluxes are heavily influenced by the reactive nature of astrocytes, which could lead to AQP4 depolarization from vascular end-feet and migrate to astrocyte parenchymal processes [46], and therefore be associated with glymphatic pathway impairment [47].

Figs. 4 and 5 show the variation of the FEM simulations on the anatomically accurate geometries. The shape of the ventricles was traced from an axial slice arising from the DICOM data described in Section 2.1. A blended coloring scheme is used for the plots in Fig. 4. The periphery of the parenchyma (with the inclusion of pronounced sulci) and periventricular region were adequately refined using a simple algorithm utilizing a combination of simplex area and individual side lengths of the triangles. Rivara refinement [48] is then used to successively improve the mesh until a termination criterion is met. The u and v components of the parenchymal displacement can be seen in Fig. 4a and b after 5 s of simulation. There is an asymmetric variation in the displacement fields of the components, and qualitative resemblance to the porohyperelastic simulations conducted by Kim et al. [49] exists in the vicinity of regions with largest ependymal wall chord length and centrum semiovale. Fig. 4c depicts the CSF/ISF increment, with visible accumulation in the periventricular regions, in addition to localized areas close to the superior occipital gyrus,
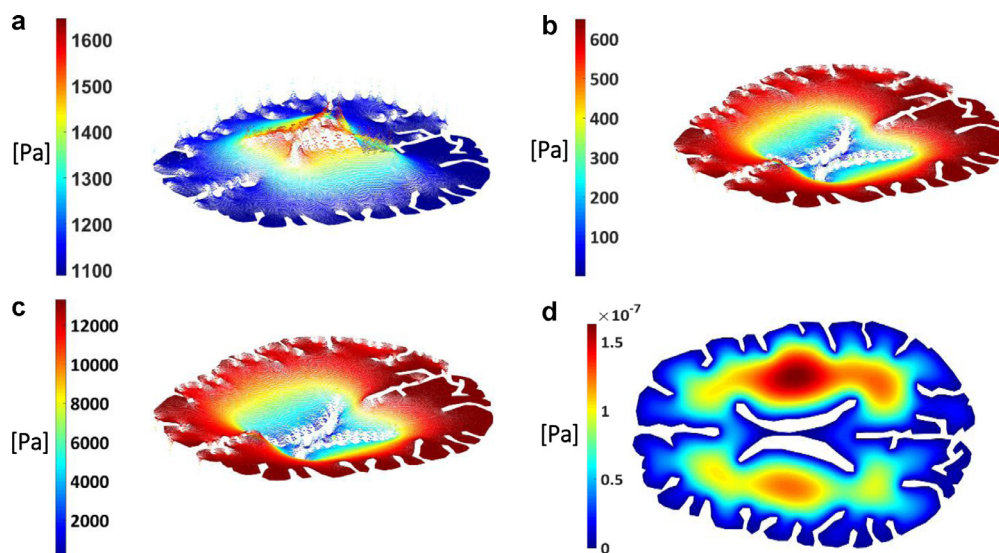
Fig. 5. Pore pressure of the four fluid compartments. (a) CSF/ISF pressure within the anatomically accurate geometry. As can be seen, higher pressures can be found in the surface of the ventricles and their vicinity. (b) Venous pressure field. There is a higher pressure found in the periphery of the parenchyma, whilst lower pressures can be found closer to the ventricle. This is due to the nature of the boundary conditions adopted for this compartment. (c) Pressure within the arterial compartment. (d) Pressure within capillary compartment. Peak pressures can be seen to persist in the parenchyma. The solution field is asymmetric in nature.

cingulate gyrus and central sulcus. What is interesting to note is that the results obtained resemble the qualitative characteristics of the work on cerebral content conducted by Levine [43], in that the larger the ventricular displacement, the gradient of transparenchymal CSF content tends to reduce, especially if the rate of pressure increase is too rapid. In our simulations, the pressure on the ventricle wall was linearly increased between 1088.8 and 1645.9 Pa within 5 s to simulate this process. Periventricular lucency (first witnessed by Naidich et al. [50]) is represented by increased CSF content in the periventricular regions, and is assumed to result from ependymal surface breakdown which helps alleviate some of the pressure in the ventricles by allowing for some CSF extravasation (and oedema formation). This mechanism could be achieved with the possible assistance of AQP4 [19], which lines the ependymal surface. Peña et al. [36] theorize that the concavity of the ventricles helps accumulate expansive stresses on the horns of the ventricles, which as is now known could induce swelling activated Cl^- channels such in microglia [17,51] and facilitate periventricular lucency (PVL) due to the effects on void ratio. Developments in Fluid-attenuation inversion recovery magnetic resonance (FLAIR MR) imaging allow for the more accurate justification of PVL and interstitial oedema, since it must be distinguished from *ependymitis granularis*, which incorporates increased fluid content, decreased myelin or breakdown of the ependymal lining accompanied by gliosis [14]. The different grading scales described by Ho et al. [14] insinuate that further information is required (such as a diffusion tensor imaging map) in such circumstances. A further point to note is that the components of the displacement incorporate weighted contributions of the pressure gradient of each of the fluid compartments. This means that the varying set of boundary conditions for the different compartments along with the updating source terms contribute to the asymmetric nature of the displacement fields.

In Fig. 4d, there is clear evidence of peak filtration velocity being localized in every sulcus and frontal and the temporal horns of the ventricles. These velocities can be as much as two orders of magnitude higher than the minimum velocities found in the dark ring surrounding the ventricles. This capillary filtration velocity field is qualitatively similar to the velocity field of the other compartments. Shahim et al. [52] and Wirth and Sobey [5] also showed that increased filtration velocity persists around the ventricular horns of their first patient case (homogeneous and isotropic simulation). The low

magnitudes are merely a consequence of the theoretical boundary conditions that have been imposed on the surface of the ventricles and parenchyma (Eq. (4)c). The capillary network resistance to the flow from the capillary compartment is given a value (see Table 1) that is relatively large (as in other work [1–3]), and it is also the case that the omission of a pulsatile CSF production rate (although this is within the capability of the FEM template) also contributes to the low filtration velocity and pore pressure in the capillary compartment.

The pressure distributions (Fig. 5a–d) in the cerebroventricular region after 5 s depict intuitive characteristics, since the pore pressure fields for the four fluid compartments are closely aligned to the boundary conditions that are imposed on the system. It is also important to appreciate that the various sets of source and sink terms vary in magnitude between compartments and also evolve dynamically with each time step.

In this work, the limitations surrounding the models include the fact that a spherically symmetric geometry was used to conceptualize the development of the 1D FDM based MPET template. This required the amalgamation of the cerebroventricular system into one node within the 1D MPET discretization. Capturing the individual dilation of the segments of the ventricles was therefore not possible. The quasi-steady assumption in the 1D-MPET template also negates the effects of pulsatility in the blood and CSF/ISF compartments. Altered pulsatility in the cerebral environment can be investigated in full detail once the fully dynamic MPET system is implemented [62]. An additional assumption is that of a rigid ventricular wall in the CFD simulations. Ventricular surface motion is expected to alter the CSF dynamics significantly, especially in light of pulsatility in the aforementioned compartments.

The MPET field equations are based on linearized elasticity, and it is noted that Taylor and Miller [35] provide sound reasoning why this constitutive relationship is adequate for the study of HCP. With the time scales associated with the inclusion of the inertial terms (cardiac pulsations or respiration), the use of viscoelasticity (or poroviscoleasticity) will need to be used as a constitutive relation. Under very large strains, which would be accompanied by substantial (and asymmetric) ventriculomegaly, a non-linearly elastic or poroviscoelastic [53,54] constitutive law should also be assessed.

The compartmental foundation of the current MPET system may well have to be augmented to account for the added spatial

dimensionality in the transfer of fluid between the various blood and CSF/ISF compartments. As hydrostatic pressure is the driving force behind these terms, the current MPET framework does not take into account any osmotic or oncotic effects. The MPET framework could strive to be augmented in a manner that would allow the investigation of capturing the Donnan effect [16,55]. Important contributions on this front have recently been made by Elkin et al. [56] and Lang et al. [57]. The latter work used a steady-state triphasic model for soft tissue, which couples the effects of ion concentration and fluid pressure with elastic deformation of the tissue, allowing for osmotic effects to drive tissue swelling.

A further constraint on the system was on the directionality of inter-compartmental fluid transfer. These restrictions will have to be relaxed when considering recent advances in CSF hydrodynamics [47,58]. This work assumed that the outflow of CSF/ISF to the sagittal sinuses was equal to production of CSF/ISF from the choroid plexuses. This inherently implies that any fluid content accumulation in the model comes from a physiological change within the parenchyma. Such an assumption is not unreasonable when considering overall allostasis, however it is an assumption nevertheless.

Darcy's law was used as it was assumed that flow in the porous medium is laminar with low Reynolds number. However, it can be envisaged that at very low percolation speeds, the interaction between the fluid filled pores and surrounding matrix becomes increasingly important, and other more detailed applications of Darcy's law could be investigated [59]. The MPET template can accommodate more elaborate transport laws, which may better suit the specific rheology of the parenchymal medium. Distinction and interaction between different transport laws can for instance be made between white and grey matter, since it is known these would display separate anisotropic characteristics which could be served by more detailed fluid flux representations [60,61]. It is also noted that the same value of c_{ε} [6] was used throughout all fluid compartments, owing to the limited experimental data that exists for the remaining compartments (a, c, v). Finally, the components of ventricular displacement were constrained by a simple rigid skull boundary condition on the periphery of the parenchyma.

5. Conclusion

This study has outlined the application of a multicompartmental poroelastic framework to investigate interstitial oedema formation and its alleviation, using a simple 1D model. Interstitial oedema formation was initially enforced via the enlargement of an anatomically accurate interconnected cerebroventricular system when under the influence of fourth ventricle outlet obstruction. Endoscopy directed at the blocked outlets was found to alleviate the symptoms, and reduce ventriculomegaly within the range of what is expected for a healthy patient. The capacity of monitoring CSF/ISF accumulation in the periventricular region was also investigated with the aid of a two-dimensional FEM numerical template. Through the enforcement of relevant boundary conditions that mimic ventricular expansion, the asymmetric nature of the effects of ventricular enlargement (on the components of displacement) along with compartmental pressures and fluid content could be obtained. The latter gave rise to interesting observations relating to periventricular lucency.

Conflict of interest

No conflict of interest.

References

[1] Tully B, Ventikos Y. Cerebral water transport using multiple-network poroelastic theory: application to normal pressure hydrocephalus. J Fluid Mech 2011;667:188–215.

[2] Vardakis JC, Tully BJ, Ventikos Y. Multicompartmental Poroelasticity as a platform for the integrative modeling of water transport in the brain. In: Holzapfel GA, Kuhl E, editors. Computer models in biomechanics. Netherlands: Springer; 2013. p. 305–16.

[3] Vardakis JC, Tully BJ, Ventikos Y. Exploring the efficacy of endoscopic ventriculostomy for hydrocephalus treatment via a multicompartmental poroelastic model of CSF transport: a computational perspective. PLoS One 2013;8(12):e84577.

[4] Smillie A, Sobey I, Molnar Z. A hydroelastic model of hydrocephalus. J Fluid Mech 2005;539:417–43.

[5] Wirth B, Sobey I. An axisymmetric and fully 3D poroelastic model for the evolution of hydrocephalus. Math Med Biol 2006;23:1–26.

[6] Li X, von Holst H, Kleiven S. Influences of brain tissue poroelastic constants on intracranial pressure (ICP) during constant-rate infusion. Comput Methods Biomech Biomed Eng 2013;16(12):1330–43.

[7] Rekate HL. A contemporary definition and classification of hydrocephalus. Semin Pediatr Neurol 2009;16(1):9–15.

[8] Wilson R, Williams M. Disorders of intracranial pressure and cerebrospinal fluid circulation. In: Irani D, editor. Cerebrospinal fluid in clinical practice. Philadelphia: Saunders Elsevier; 2009. p. 99–104.

[9] Thompson D. Hydrocephalus. Neurosurgery 2009;27(3):130–4.

[10] Corns R, Martin A. Hydrocephalus. Neurosurgery 2012;30(3):142–8.

[11] Bech-Azeddine R, Gjerris F. idiopathic normal pressure hydrocephalus. Cerebrospinal fluid disorders. CRC Press; 2009. p. 284–99.

[12] May P, Sgouros S. Treatment of hydrocephalus in the modern era (1950s-current date). In: Mallucci C, Sgouros S, editors. Cerebrospinal fluid disorders. New York: Informa Healthcare USA, Inc; 2010. p. 63–109.

[13] Raslan A, Bhardwaj A. Medical management of cerebral edema. Neurosurg Focus 2007;22(5):E12.

[14] Ho M-L, Rojas R, Eisenberg RL. Cerebral edema. Am J Roentgenol 2012;199(3):W258–73.

[15] Donkin JJ, Vink R. Mechanisms of cerebral edema in traumatic brain injury: therapeutic developments. Curr Opin Neurol 2010;23(3):293–9.

[16] Goriely A, et al. Mechanics of the brain: perspectives, challenges, and opportunities. Biomech Model Mechanobiol 2015;15(5):1–35.

[17] Fukuda A, Badaut J. Aquaporin 4: a player in cerebral edema and neuroinflammation. J Neuroinflamm 2012;9(1):1–9.

[18] Fukuda AM, et al. Delayed increase of astrocytic aquaporin 4 after juvenile traumatic brain injury: possible role in edema resolution? Neuroscience 2012;222:366–78.

[19] Papadopoulos MC, Verkman AS. Aquaporin water channels in the nervous system. Nat Rev Neurosci 2013;14(4):265–77.

[20] Thrane AS, Rangroo Thrane V, Nedergaard M. Drowning stars: reassessing the role of astrocytes in brain edema. Trends Neurosci 2014;37(11):620–8.

[21] Spennato P, et al. Endoscopic third ventriculostomy for idiopathic aqueductal stenosis. World Neurosurg 2013;79(2):S21.e13–S21.e20.

[22] Hellwig D, et al. Endoscopic third ventriculostomy for obstructive hydrocephalus. Neurosurg Rev 2005;28:1–34.

[23] Ferrer A, Notaris Md. Third ventriculostomy and fourth ventricle outlets obstruction. World Neurosurg 2012;79(2):S20.e9–S20.e13.

[24] Mugamba J, Stagno V. Indication for ETV. World Neurosurg 2012;79(2):S20.e19–S20.e23.

[25] Woodworth GF, et al. Predictors of surgery-free outcome in adult endoscopic third ventriculostomy. World Neurosurg 2012;78(3-4):312–17.

[26] Vogel TW, et al. The role of endoscopic third ventriculostomy in the treatment of hydrocephalus. J Neurosurg: Pediatr 2013;12(1):54–61.

[27] Rangel-Castilla L, Barber S, Zhang YJ. The role of endoscopic third ventriculostomy in the treatment of communicating hydrocephalus. World Neurosurg 2012;77(3–4):555–60.

[28] Grotenhuis JA, Al-Kheshen SMA-S, Mohammed KE. Endoscopy for Hydrocephalus—General Aspects. In: Mallucci C, Sgouros S, editors. Cerebrospinal Fluid Disorders. New York: Informa Healthcare USA, Inc; 2010. p. 496–507.

[29] Decq P, et al. A new device for endoscopic third ventriculostomy. J Neurosurg 2000;93:509–12.

[30] Mohanty A, et al. Efficacy of Endoscopic Third Ventriculostomy in fourth ventricular outlet obstruction. Neurosurgery 2008;63(5):905–14.

[31] Nagashima T, Shirakuni T, Rapoport SI. A two-dimensional, finite element analysis of vasogenic brain edema. Neurol Med–Chirur 1990;30(1):1–9.

[32] Nagashima T, et al. Biomechanics of vasogenic brain edema application of biot's consolidation theory and the finite element method. In: Inaba Y, Klatzo I, Spatz M, editors Brain edema. Berlin, Heidelberg: Springer; 1985. p. 92–8.

[33] Nagashima T, et al. Biomechanics of hydrocephalus: a new theoretical model. Neurosurgery 1987;21(6):898–904.

[34] Nagashima T, et al. Formation and resolution of brain edema associated with brain tumors. A comprehensive theoretical model and clinical analysis. Acta Neurochir Suppl (Wien) 1994;60:165–7.

[35] Taylor Z, Miller K. Reassessment of brain elasticity for analysis of biomechanisms of hydrocephalus. J Biomech 2004;37(8):1263–9.

[36] Peña A, et al. Effects of brain ventricular shape on periventricular biomechanics: a finite-element analysis. Neurosurgery 1999;45(1).

[37] Biot MA. General theory of three-dimensional consolidation. J Appl Phys 1941;12(2):155–64.

[38] Detournay E, Cheng AH-D. Fundamentals of poroelasticity. In: Fairhurst C, editor. Comprehensive rock engineering: principles, practice and projects, vol. II, analysis and design method. Pergamon Press; 1993. p. 113–71.

[39] Ferziger JH, Peric M. Computariomal methods for fluid dynamics. 3rd ed. Germany: Springer-Verlag; 2002.

[40] Tully B, Ventikos Y. Coupling poroelasticity and CFD for cerebrospinal fluid hydrodynamics. IEEE Trans Biomed Eng 2009;56(6):1644–51.

[41] Freund RW. A transpose-free quasi-minimal residual algorithm for non-Hermitian linear systems. SIAM J Sci Comput 1993;14(2):470–82.

[42] Sobey I, Wirth B. Effect of non-linear permeability in a spherically symmetric model of hydrocephalus. Math Med Biol 2006;23:339–61.

[43] Levine DN. the pathogenesis of normal pressure hydrocephalus: a theoretical analysis. Bull Math Biol 1999;61:875–916.

[44] Levine DN. Ventricular size in pseudotumor cerebri and the theory of impaired CSF absorption. J Neurol Sci 2000;177(2):85–94.

[45] Levine DN. Intracranial pressure and ventricular expansion in hydrocephalus: Have we been asking the wrong questions? J Neurol Sci 2008;269(1-2):1–11.

[46] Kress BT, et al. Impairment of paravascular clearance pathways in the aging brain. Ann Neurol 2014;76(6):845–61.

[47] Jessen NA, et al. the glymphatic system: a beginner's guide. Neurochem Res 2015;40(12):2583–99.

[48] Rivara MC. Algorithms for refining triangular grids suitable for adaptive and multigrid techniques. Int J Numer Methods Eng 1984;20(4):745–56.

[49] Kim H, et al. Porohyperelastic anatomical models for hydrocephalus and idiopathic intracranial hypertension. J Neurosurg 2015;122(6):1330–40.

[50] Naidich TP, et al. Evaluation of pediatric hydrocephalus by computed tomography. Radiology 1976;119(2):337–45.

[51] Schlichter LC, Mertens T, Liu B. Swelling activated Cl- channels in microglia: biophysics, pharmacology and role in glutamate release. Channels (Austin) 2011;5(2):128–37.

[52] Shahim K, et al. Finite element analysis of normal pressure hydrocephalus: influence of CSF content and anisotropy in permeability. Appl Bionics Biomech 2010;7(3):187–97.

[53] Mehrabian A, Abousleiman Y. General solutions to poroviscoelastic model of hydrocephalic human brain tissue. J Theor Biol 2011;291(0):105–18.

[54] Bemer E, et al. Poromécanique: de la poroélasticité linéaire à la poroélasticité non linéaire et la poroviscoélasticité. Oil Gas Sci Technol – Rev IFP 2001;56(6):531–44.

[55] Donnan FG. The theory of membrane equilibria. Chem Rev 1924;1(1):73–90.

[56] Elkin BS, Shaik MA, Morrison B. Fixed negative charge and the Donnan effect: a description of the driving forces associated with brain tissue swelling and oedema. Philos Trans Ser A Math Phys Eng Sci 2010;368(1912):585–603.

[57] Lang GE, et al. Is the Donnan effect sufficient to explain swelling in brain tissue slices? J R Soc Interface 2014;11(96):20140123.

[58] Chikly B, Quaghebeur J. Reassessing cerebrospinal fluid (CSF) hydrodynamics: a literature review presenting a novel hypothesis for CSF physiology. J Bodyw Mov Ther 2013;17(3):344–54.

[59] Shenoy AV. Darcy–Forchheimer natural, forced and mixed convection heat transfer in non-Newtonian power-law fluid-saturated porous media. Transp Porous Media 1993;11(3):219–41.

[60] Feng Y, et al. Measurements of mechanical anisotropy in brain tissue and implications for transversely isotropic material models of white matter. J Mech Behav Biomed Mater 2013;23(0):117–32.

[61] Hansen MB, et al. Using diffusion anisotropy to characterize neuronal morphology in gray matter: the orientation distribution of axons and dendrites in the NeuroMorpho.org database. Front Integr Neurosci 2013;7. Article 31, Pages 1–13.

[62] Chou D, Vardakis JC, Guo L, Tully BJ, Ventikos Y. A fully dynamic multicompartmental poroelastic system: Application to aqueductal stenosis. J Biomech 2015.